Original article

Textile Research Journal
0(00) 1–13

DOI: 10.1177/0040517514525876
trj.sagepub.com

Frictional behavior of carbon fiber tows: a contact mechanics model of tow–tow friction

Bo Cornelissen[1], Matthijn B de Rooij[2], Bert Rietman[1] and Remko Akkerman[1]

Abstract
Composite-forming processes involve mechanical interactions at the ply, tow, and filament level. The deformations that occur during forming processes are governed by friction between the contacting tows on the mesoscopic level and consequently between filaments on the microscopic level. A thorough understanding of the frictional properties at the level of individual filaments is essential to understand and to predict the macroscopic deformations of a textile reinforcement during forming. This work presents a contact mechanics modeling approach to provide a theoretical background of the frictional behavior of dry fibrous tows in contact with each other. The predicted frictional behavior is in qualitative and quantitative agreement with experimentally observed frictional forces of carbon fiber tows in sliding contact. The relative orientation of the contacting tows is of great importance for the developed frictional forces in the contact.

Keywords
friction, tow, yarn, capstan, filament

High performance fibrous tows mainly find their application in structural composites, which consist of a thermoplastic or thermoset matrix and continuous fibrous tows for reinforcement. These continuous fibrous tows deform during the forming phase of production processes, for example when draping dry fabric prior to resin transfer molding (RTM). The tows conform to the local shape of the tool surface on which the composite part is being manufactured. Usually, several plies are used in a composite part, which also leads to inter-tow contacts. Local cross-sectional changes occur in the tow due to the induced loads, which are mainly transferred in the form of friction. The tow orientation and the filament distribution affect the mechanical properties of the composite part to a large extent. Knowledge of the tow orientation and tow deformation behavior is therefore essential to control the desired product quality in terms of mechanical performance, dimensional accuracy, and visual appearance.

The frictional behavior of fibrous tows during processing typically involves intra-tow (on the microscopic filament scale), inter-tow, and tow–metal interactions. This work deals with the frictional behavior of the inter-tow system, i.e. the frictional behavior of tow–tow contacts. A study on the frictional behavior of tow–metal contact is described in another paper.[1]

Several researchers have investigated the frictional behavior of contacting fibrous tows.[2–8] These experiments were performed on different setup types for a variety of experimental parameters. In 2009, Yuksekkaya provided an overview describing the majority of these experiments.[9]

Experimental work on the frictional behavior of fibrous tows showed that inter-filament friction and surface interactions determine the deformation

[1]Department of Production Technology, University of Twente, the Netherlands
[2]Department of Surface Technology and Tribology, University of Twente, the Netherlands

Corresponding author:
Bo Cornelissen, Department of Production Technology, Faculty of Engineering Technology, University of Twente, P.O. box 217, 7500 AE Enschede, the Netherlands.
Email: b.cornelissen@utwente.nl

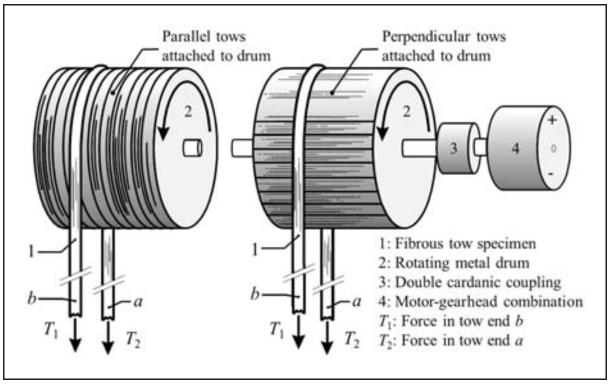

Figure 1. Schematic description of the capstan experiment for friction characterization of fibrous tows. A tow specimen is wrapped around a friction drum on which tows of the same material are attached in either a parallel (left) or perpendicular (right) orientation.

behavior of the fibrous tows.[10] Capstan experiments consisted of measuring forces in the ends of fibrous tow specimens wrapped around a rotating friction drum covered with fibrous tow material. This setup is schematically illustrated in Figure 1. The current work proposes a contact mechanics modeling approach of tow friction to provide a theoretical understanding of the observed behavior.

A model for the contact mechanics of fibrous tows during forming is proposed in the next section. The scope of the model and material properties are explained, followed by a derivation of typical loading conditions for tow material, based on a capstan friction experiment. Subsequently, a contact mechanics approach is proposed to determine the contact area for both perpendicular and parallel sliding tow contact. The effect of adhesion on the developed frictional force between perpendicular tows in sliding contact is also assessed. The model results are presented in the results section, followed by a comparison with experimental data in the discussion section to validate the model.

Contact mechanics modeling approach

This section deals with the model assumptions and presents the contact mechanics approach of the contact area between tows in sliding contact.

Scope of the modeling approach

The contact mechanics approach of tow deformation behavior is based on the relation between the exerted compressive load on sliding filaments in fibrous tows and the developed frictional force. The area of contact between the filament and the fibrous counterface is load dependent.[11–13] Consequently, this results in a load dependency of the frictional force between the tow and the counterface. Howell and Mazur proposed the following empirical friction law:[11]

$$F_{\mathrm{f}} = kN^n, \tag{1}$$

where N is the applied normal load on the contacting body (in this case a tow that consists of many filaments). Gupta and Mogahzy gave the fitting parameters k and n a theoretical background by stating that in the case of fibrous materials the index n is governed by the (visco) elastic properties of the junctions in the contacting asperities under compression,[12,14] implying that n is not necessarily equal to 1, which corresponds to purely plastic deformation of the junctions in the contact locations. The value of k is determined by chemical, physical, and morphological properties of the filament material and the filament–counterface contact dimensions.

Roselman and Tabor described the frictional behavior of single carbon filaments in contact in the 1970s.[15,16] The friction equation consists of a shear friction part involving the product of a real contact area A_{r} between the contacting filaments with an interfacial shear strength τ, and a ploughing part P:

$$F_{\mathrm{f}} = A_{\mathrm{r}}\tau + P. \tag{2}$$

Analogously, we assume that the same friction relation describes the frictional force F_{f} between fibrous tows in sliding contact. However, in the current modeling approach we assume that all deformations at the asperity level take place in the elastic regime. It is assumed that the ploughing part of friction is caused by plastic deformation at the level of asperities only; therefore, this ploughing part P is neglected. Furthermore, it is assumed that the interfacial shear strength τ is a material property, which is independent of the relative orientation of the filaments in the tows.

Material

The tow–tow contacting behavior was modeled for carbon fiber tow material, for which experimental data of both perpendicular and parallel contact friction was obtained.[10] Table 1 lists the relevant properties of the carbon fiber tows. The fibrous tows received a thermal treatment to remove the applied surface finish (epoxy based).

Figure 2 shows a scanning electron microscopy (SEM) micrograph of a typical carbon filament. The surface topography of the carbon filament consists of ridges in the axial filament direction. The typically observed radius of curvature R_{ridge} of approximately 100 nm is comparable to the value of $R_{\mathrm{ridge}} \approx 200$ nm

Table 1. Manufacturer data (M) of the Torayca T300JB carbon tow material used in the contact model. Additional data of equivalent carbon tow material from literature sources is indicated with the corresponding reference

Description	Symbol	Unit	Value	Ref.
Density	ρ	kg/m^3	1780	M
No. of filaments in the tow	n	–	3000	M
Filament radius	R_{fil}	μm	3.5	Ueda and Takiguchi,[17] M
Axial elastic modulus	E_{axial}	GPa	230	Ueda and Takiguchi,[17] M
Transverse elastic modulus	E_{trans}	GPa	15	Maurin et al.[18]
Transverse Poisson coefficient	ν	–	0.445	Ueda and Takiguchi[17]
Work of adhesion	w	mJ/m^2	95.1	Luo et al.[19]
C–C interatomic spacing	z_0	Å	1.54	Shackelford[20]

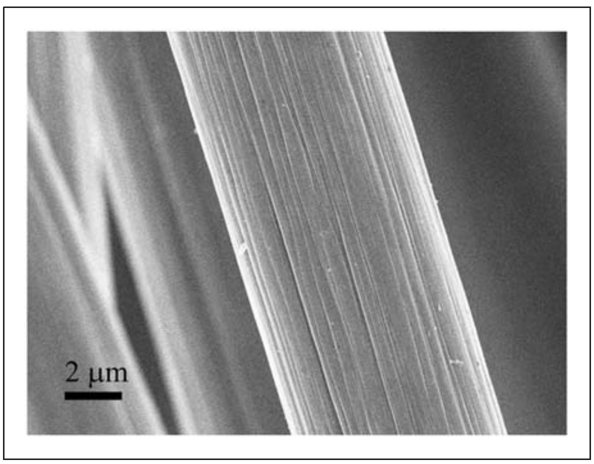

Figure 2. Micrograph (SEM) of a carbon filament with a typical diameter of 7.0 μm. The ridges in the axial filament direction are clearly visible; the radius of curvature R_{ridge} is approximately 100 nm.

reported by Roselman and Tabor.[15] These dimensions apply to the specific type of carbon fibers used in this research. Note that the ridge dimensions of other types of carbon filaments, such as pitch-based variants or filaments from a different manufacturer, can deviate from the dimensions reported here. The specific geometry in this work is used as a ball-park figure and it is not intended to represent a wide variety of carbon filaments.

From tow to filament load

The typical compressive load acting on a single filament is derived from actual measurement data, obtained in the aforementioned capstan friction experiment.[10] Figure 1 illustrates the experiment schematically. A fibrous tow was draped on a metal friction drum, having a radius $R_{drum} = 25.0$ mm, with a known wrapping angle θ_{wrap}. The tensile tow end loads T_1 at $\theta_1 = 0$ and T_2 at $\theta_2 = \pi$ [rad] were measured. An apparent coefficient of friction μ_{app} can be obtained from the capstan relation:

$$\mu_{app} = \ln\left(\frac{T_2}{T_1}\right)\frac{1}{\theta_{wrap}}. \tag{3}$$

Amontons' first law is the main underlying assumption in the capstan equation, stating that the frictional force F_f between the tow and the friction drum is directly proportional to the normal load $N(\theta)$ (in newtons) exerted on the tow by the friction drum:

$$F_f = \mu_{app} N(\theta). \tag{4}$$

The description of equation (4) is also known as Coulomb friction and will be referred to as Amontons–Coulomb friction from here. The tensile tow load at any arbitrary angle θ follows from the known ingoing tensile load T_1 and the apparent coefficient of friction given by equation (3):

$$T(\theta) = T_1 \exp\left(\mu_{app}\theta\right). \tag{5}$$

The estimation of $T(\theta)$ in equation (5) assumes Amontons–Coulomb friction, although a non-Amontons–Coulomb type of behavior for tow friction was mentioned before in equation (1). However, the load range in which the individual capstan measurements took place was relatively small and thus the difference between the uniform apparent coefficient of friction μ_{app} from equation (4) and the Howell behavior of equation (1) is relatively small as well. Therefore, the straightforward friction behavior relation of equation (5) was used for the normal load derivation in this work.

The distributed normal load N_{tow} (in N/m arc length) in the contact between the stationary and moving tows follows directly from load equilibrium of an infinitesimal part of the stationary tow, Appendix 1 contains the derivation:

$$N_{\mathrm{tow}}(\theta) = \frac{T_{\mathrm{tow}}(\theta)}{R_{\mathrm{drum}}}. \tag{6}$$

An estimation of the number of filaments in direct contact with each other is required to calculate the distributed normal load on a filament N_{fil} (θ) along the wrapped length $l_{\mathrm{wrap}} = \theta_{\mathrm{wrap}}$ R_{drum}. Assuming a close packing of filaments, the normal load in the stationary tow is transferred from one layer of filaments to the layer beneath. The bottom layer of filaments, i.e. the layer in direct contact with the filaments from the moving tow, transfers the normal load, as illustrated in Figure 3. The amount of contacting filaments n_{fil} for each tow material was estimated from observations of the contacting tow shape during capstan experiments.[10] The transferred normal loads from filament layer to filament layer are assumed to be uniformly distributed along the filaments of the bottom layer as a first approximation. In the actual situation, the load distribution depends on the cross-sectional geometry of the tow as well as the packing of the filaments. The distributed normal load on the individual contacting filaments of the stationary tow in the capstan setup then becomes:

$$N_{\mathrm{fil}}(\theta) = \frac{N_{\mathrm{tow}}(\theta)}{n_{\mathrm{fil}}}. \tag{7}$$

Contact area calculations based on N_{fil} level are described in the following two subsections for perpendicular, parallel, and nearly parallel filament contacts.

Perpendicular tow contact

The contact between filaments with radius R_{fil} under a perpendicular orientation is modeled with two crossed cylinders, as illustrated in Figure 4. The radius of curvature of the capstan friction drum $R_{\mathrm{drum}} = 25.0$ mm is large compared to the filament radius $R_{\mathrm{fil}} = 3.5$ µm and is therefore approximated by a flat surface. Using a contact mechanics analogy, the crossed cylinders can be represented by a sphere indenting a plane. The principal reduced radius of curvature R_{m} of the equivalent contact is defined as:

$$R_{\mathrm{m}} = \left(\frac{1}{R_{\mathrm{x1}}} + \frac{1}{R_{\mathrm{y1}}} + \frac{1}{R_{\mathrm{x2}}} + \frac{1}{R_{\mathrm{y2}}}\right)^{-1}. \tag{8}$$

where $R_{\mathrm{x1}} = R_{\mathrm{x2}} = R_{\mathrm{fil}}$ and $R_{\mathrm{y1}} = R_{\mathrm{y2}} = \infty$. This parameter R_{m} translates all curvatures in the two-body contact to one spherical body in contact with a flat surface.[21] The sphere indents an elastic half-plane, as illustrated in Figure 4. In this first approximation of the contact, the filament surface is assumed to be smooth, i.e. without any surface irregularities.

The compressive load P_{perp} on the sphere in the contact analogy is a load in newtons. This force is derived from the local normal filament load in equation (7). Multiplication of $N_{\mathrm{fil}}(\theta)$ with a projected arc length corresponding to one crossing filament diameter leads to the load (in newtons) of the perpendicular contact at the angular coordinate θ:

$$P_{\mathrm{perp}}(\theta) = 2R_{\mathrm{fil}} N_{\mathrm{fil}}(\theta). \tag{9}$$

Equation (2) relates the theoretical frictional force in a sliding contact between filaments to the real contact area A_{r}. The sphere-on-a-plane contact analogy provides a means to calculate A_{r}. The radius of the contact area between a sphere under the compressive load $P_{\mathrm{perp}}(\theta)$ on an elastic half-plane for Hertzian contact is:[21]

$$a_{\mathrm{p}} = \left(\frac{3P_{\mathrm{perp}}(\theta) R_{\mathrm{m}}}{2E^*}\right)^{1/3}, \tag{10}$$

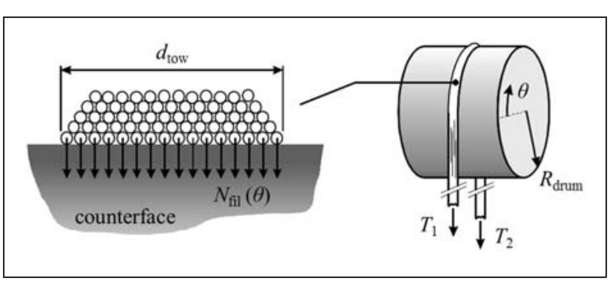

Figure 3. Uniform normal load distribution assumption of the bottom filaments of the stationary fibrous tow. The contacting counterface tows are oriented perpendicularly or parallel to the stationary tow. Note that the friction drum rotates in the opposite direction of θ (as illustrated in Figure 1).

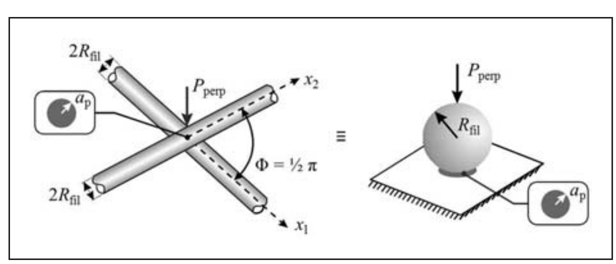

Figure 4. Schematic illustration of filaments in perpendicular contact. The contact between the filaments is represented by the analogy of a sphere indenting an elastic half-plane. The contact area A_{p} is circular with contact radius a_{p}.

where E^* represents the reduced modulus of elasticity of the two filaments in contact:

$$E^* = \left(\frac{1-\nu_1^2}{E_1} + \frac{1-\nu_2^2}{E_2}\right)^{-1}. \quad (11)$$

Because the contacting filaments are made of the same material, with the transverse moduli of elasticity $E_1 = E_2 = E_{\mathrm{trans}}$ and the Poisson ratios $\nu_1 = \nu_2 = \nu$, equation (11) reduces to:

$$E^* = \left(\frac{2\left(1-\nu^2\right)}{E_{\mathrm{trans}}}\right)^{-1}. \quad (12)$$

This representation of the reduced modulus implies isotropic material behavior, although carbon filaments are known to have an orthotropic nature. However, for reasons of simplicity and within the scope of the current modeling approach, an isotropic formulation using the transverse modulus of elasticity of the carbon filaments is applied.

The relevant material properties are listed in Table 1. The obtained circular contact area $A_p = \pi\, a_p^{\,2}$ is a first approximation due to the smooth filament surface assumption. This first approximation does not account for the presence of the ridges on the filament surface, illustrated in Figure 2. The typical radius of curvature of the ridge of approximately 100 nm is small compared to the filament radius. Based on the dimension of the first approximation contact radius a_p, the perpendicular contact between carbon filaments can take place at one or two ridges. Calculating the contact area between these ridges should therefore provide a more realistic representation of the perpendicular tow friction experiment. For that purpose, the carbon filament-filament contact areas as a function of load are also modeled for the radius of a ridge R_{ridge}. Figure 5 illustrates the contact analogies for two situations, i.e. the contact between one ridge on each filament, denoted 1×1, and the contact between two ridges on each filament, denoted 2×2. The 1×1 contact analogy is equivalent to the aforementioned case of the contact of smooth filaments. The 2×2 contact of ridges was modeled by evenly distributing the load P_{perp} over four individual contact areas. The resulting contact radii are $a_{p,1\times1}$ and $a_{p,2\times2}$. Additionally, 1×1 ridge contact calculations for $R_{\mathrm{ridge}} = 200$ nm were performed to assess the sensitivity of the predicted contact area to the radius of a ridge. The results of the contact calculations as a function of the distributed normal filament load are interpreted in the discussion section.

Furthermore, a Maugis–Dugdale (MD) contact analysis provides insight into the contribution to the contact area of adhesion between the filaments.[22–24] The carbon fiber material in this work is relatively soft compared to metals. Johnson and Greenwood showed that attractive forces due to adhesion between contacting materials can have a significant effect on the real contact area and thus the theoretical frictional force between contacting filaments.[23] Different models exist to account for this adhesion effect.[22–24] The contact of most (technical) fibrous materials is well represented by the Maugis–Dugdale model, which is based on several filament properties: the work of adhesion, the transverse stiffness, and the geometry.[22,23] The attractive forces between the filaments result in a non-zero contact area without an externally applied load. Therefore, the contact radius a_{MD} obtained from the Maugis–Dugdale analysis is larger than the Hertzian equivalent, which does not account for the effect of adhesion between the contacting filaments. The procedure to obtain the load–area relation for adhesive contact according to Maugis–Dugdale is presented in Appendix 2.

Summarizing, the contact between perpendicularly oriented filaments is investigated for three different surface geometries represented by $R_{\mathrm{fil}} = 3.5\,\mu\mathrm{m}$ for a smooth filament surface assumption, and $R_{\mathrm{ridge}} = 100$ nm as well as $R_{\mathrm{ridge}} = 200$ nm when accounting for surface irregularities on the carbon filaments as illustrated in Figure 2. A variation of the amount of contacting ridges was taken into account; this is illustrated schematically in Figure 5. The contact calculations were performed with (MD) and without (Hertz) accounting for the contribution of adhesion between the contacting filaments. The results are presented in the next section.

Parallel and nearly parallel tow contact

A perfectly parallel orientation between the filaments of the stationary and sliding tows would result in a rectangular contact area in the axial direction of the

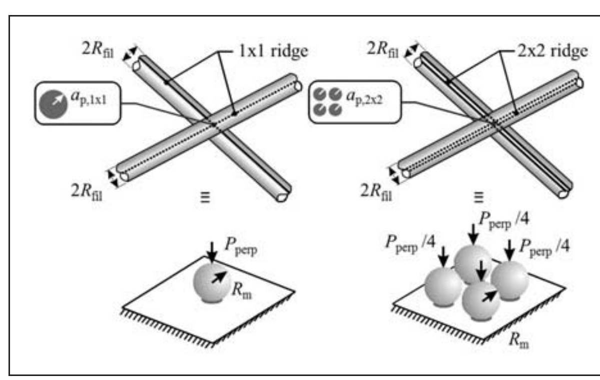

Figure 5. Analogies for the determination of the contact radii $a_{p,1\times1}$ and $a_{p,2\times2}$ of perpendicularly crossed filaments. The contact occurs between one or two ridges of each filament.

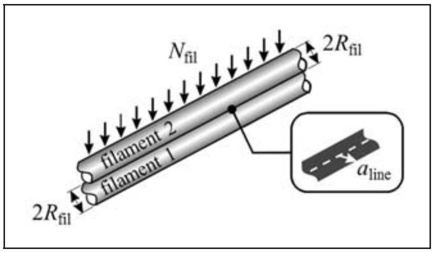

Figure 6. Perfectly parallel filament contact with the distributed normal filament load N_{fil}. The contact area is rectangular with the half-width of contact a_{line}. Filament 1 is attached to the rotating drum; filament 2 is part of the wrapped tow, which is stationary.

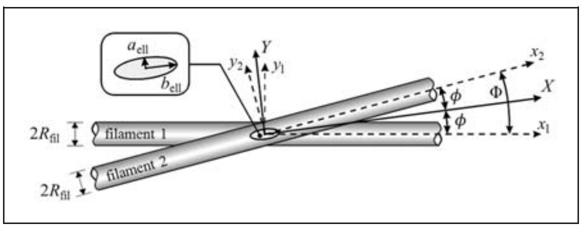

Figure 7. Oblique filament contact with the relative filament orientation $\Phi = 2\varphi$ representing the nearly parallel orientation of filaments. The contact area is elliptic with semi-minor axis a_{ell} and semi-major axis b_{ell}. Filament 1 is attached to the rotating drum; filament 2 is part of the wrapped tow, which is stationary.

filaments, as illustrated in Figure 6. For a Hertzian line contact, the half-width of contact a_{line} is:[21]

$$a_{line} = \left(\frac{4 N_{fil} R_m}{\pi E^*}\right)^{1/2}. \tag{13}$$

However, the filaments in the experimental setup contacted each other under a small angle, as illustrated in Figure 7. The estimated relative orientation of the filaments Φ was obtained from experimental observations. The filaments in the stationary wrapped tow crossed a number $n_{oblique}$ of moving filaments as a result of the relative orientation. This relative orientation originates from the fact that the stationary tow was wound on the friction drum. The winding pitch of the tow on the drum is equal to the tow width d_{tow}. Thus, a filament from the stationary tow, which is wrapped with $\theta_{wrap} = \pi$ around the moving tow/friction drum arrangement, crosses the number of filaments $n_{oblique}$ in half of the tow width d_{tow}. Consequently, the number of filaments in contact follows from half the tow width divided by the filament diameter $2R_{fil}$:

$$n_{oblique} = \frac{1}{2}\frac{d_{tow}}{2R_{fil}}. \tag{14}$$

Table 2. Tow geometry input data for the oblique tow–tow contact model, representing nearly parallel contact of the filaments

Description	Symbol	Unit	Value
No. of crossed filaments	$n_{oblique}$	–	357
Wrapping angle	θ_{wrap}	rad	π
Oblique contact angle	Φ	rad/°	0.032 / ≈2
Width of moving tow	d_{tow}	mm	5.0

Table 2 shows the appropriate values used in the tow–tow contact model. The relative orientation between the crossing filaments Φ then follows from this geometrical arrangement:

$$\Phi = \arctan\left(\frac{1}{2}\frac{d_{tow}}{l_{wrap}}\right). \tag{15}$$

This results in $\Phi \approx 2°$. The modeling procedure to account for the contact of the filaments under a relative orientation is described below.

The compressive load in newtons in each filament-to-filament contact then follows from the distributed filament load N_{fil}, derived in equation (7), multiplied by the distance between two oblique filament crossings:

$$P_{par} = N_{fil}\frac{2R_{fil}}{\sin(\Phi)}. \tag{16}$$

Analogously to the perpendicular filament-to-filament contact, the real contact area between the filaments in almost parallel orientation depends on the assumed filament surface properties. The load–area relation was calculated for the three contact geometries described in the previous subsection: $R_{fil} = 3.5\,\mu m$, $R_{ridge} = 100\,nm$, and $R_{ridge} = 200\,nm$. The general theory of oblique contact between cylindrical bodies and the contact geometry derivations are described in the literature.[21,25–27] The following equations apply when two geometrically identical cylindrical bodies contact each other under a relative angle $\Phi \neq 0$, as illustrated in Figure 7.

The contact analogy for the oblique contact of geometrically identical cylinders is that of an ellipsoidal punch with the principal relative radii of curvature R_X and R_Y which contain the translated curvatures of the contacting bodies. These radii are defined as follows:[21,27]

$$R_X = \frac{R}{1 - \cos(\Phi)}, \quad R_Y = \frac{R}{1 + \cos(\Phi)}, \tag{17}$$

where $R = R_{fil}$ for a smooth filament assumption or $R = R_{ridge}$ when the surface topography of the filament is taken into account. Furthermore, the following relation exists between the principal relative radii of curvature R_X, R_Y and the reduced radius of curvature R_m of the contacting bodies:[21,27]

$$\frac{1}{R_X} + \frac{1}{R_Y} = \left(\frac{1}{R_{x1}} + \frac{1}{R_{y1}} + \frac{1}{R_{x2}} + \frac{1}{R_{y2}}\right) = \frac{1}{R_m}. \quad (18)$$

The semi-minor axis a_{ell}, the semi-major axis b_{ell} of the elliptic contact area and the approach distance of the deformed filament surfaces in the center of the contact δ follow from the derived contact geometry and the applied normal load N_{par}, resulting in:[26]

$$a_{ell} = \alpha\left(\frac{3P_{par}R_m}{2E^*}\right)^{1/3}, \quad (19)$$

$$b_{ell} = \beta\left(\frac{3P_{par}R_m}{2E^*}\right)^{1/3}, \quad (20)$$

$$\delta = \gamma\left(\frac{9P_{par}^2}{32E^{*2}R_m}\right)^{1/3}, \quad (21)$$

where α, β, and γ are dimensionless quantities, which yield unity for a circular contact. These quantities depend on the ratio of the principal radii of curvature of the contact:

$$\zeta = \frac{R_Y}{R_X}, \quad (22)$$

where $R_Y \leq R_X$. The equations for the dimensionless quantities are presented in Appendix 3.

Summarizing, the contact between perfectly parallel ($\Phi = 0°$) and nearly parallel or obliquely ($\Phi = 2°$) oriented filaments is investigated for three different surface geometry assumptions represented by $R_{fil} = 3.5\,\mu m$ for a smooth filament surface assumption, and $R_{ridge} = 100$ nm as well as $R_{ridge} = 200$ nm when accounting for surface irregularities on the carbon filaments, as illustrated in Figure 2. A variation of the amount of contacting ridges was taken into account. The contact calculations were performed without taking the contribution of adhesion between the contacting filaments into account, i.e. using a Hertzian contact approach. The results are presented in the next section.

Results

The contact model results are presented separately for the perpendicular and parallel relative tow orientations.

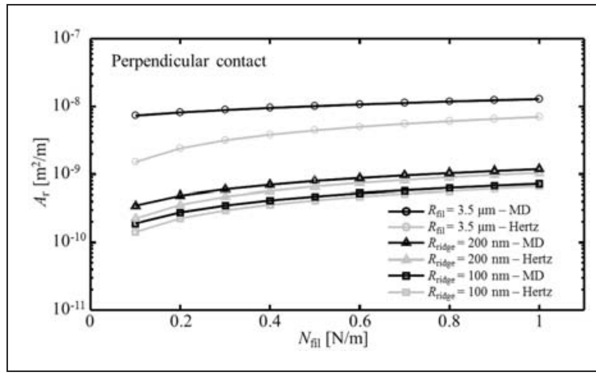

Figure 8. Contact area A_r as a function of the distributed normal filament load N_{fil} for perpendicular contact of two filaments. The contact areas are shown for three different contact geometries: $R_{fil} = 3.5\,\mu m$ represents a smooth filament-filament contact, the contact of 1x1 small ridges is represented by $R_{ridge} = 100$ nm, the contact of 1×1 large ridges by $R_{ridge} = 200$ nm. The contact areas are shown with adhesion contribution (MD, $w = 95.1$ mJ/m^2) and without adhesion contribution (Hertz).

Contact area predictions with and without accounting for surface irregularities of the filaments are presented.

Perpendicular orientation

Figure 8 shows the contact area per meter contacting filament for both the smooth filament surface assumption (R_{fil}) and the contacting ridge situations with varying R_{ridge}. The graph clearly shows the influence of the assumed contact type on the predicted real area of contact, i.e. a smooth filament (R_{fil}) versus a filament surface with ridges (R_{ridge}).

The maximum applied normal distributed load in the experiment is estimated to be 0.5 N/m. The radius of the circular contact area a_p for a smooth filament-filament contact is 99 nm at this load, the maximum pressure in the contact is 169 MPa. For the 1×1 small ridge contact, the radius a_p is 30 nm, with a maximum pressure in the contact of 1.8 GPa. A remark on the high maximum pressure for the 1×1 small ridge contact is made in the discussion section.

The adhesion contribution to the contact area is visible in Figure 8 by comparing the black curves with the grey curves with the same markers. The contribution of adhesion to the contact is larger for the smooth filament situation, i.e. the curves with the circular markers, than for the ridge-to-ridge contacts, i.e. the curves with the triangular and square markers. The dimensionless normalized load range is defined as the ratio of the absolute applied load P_{perp} and the adhesive pull-off force $2\pi w R_m$ required to separate the contacting bodies:[23]

$$\bar{P} = \frac{P_{perp}}{2\pi w R_m}. \tag{23}$$

Equation (23) shows that the effect of adhesion increases with the size of the contacting geometries, appearing in the form of R_m or a constant work of adhesion w, listed in Table 1. This explains the larger gap in Figure 8 between the Hertz and MD curves for the smooth filament assumption, i.e. $R_{fil} = 3.5\,\mu m$, than for the contact between the significantly smaller geometry of the ridges. This shows the relevance of taking the surface irregularities of the filament into account.

Parallel orientation

The real contact area as a function of the distributed filament load for tows in a nearly parallel orientation is visualized in Figure 9. The results are shown for Hertzian contact, i.e. adhesion effects were not taken into account. The black dotted curves represent the real contact area per unit filament length for a perfectly parallel orientation of the filaments, using equation (13). However, the aforementioned small relative angle of orientation $\Phi = 2^\circ$ between the contacting filaments is expected to provide a more realistic representation of the experiment. The gray curves in Figure 9 were obtained by calculating the elliptic contacts along the wrapped length of a filament using the general Hertzian elliptic contact theory, explained in the previous section.

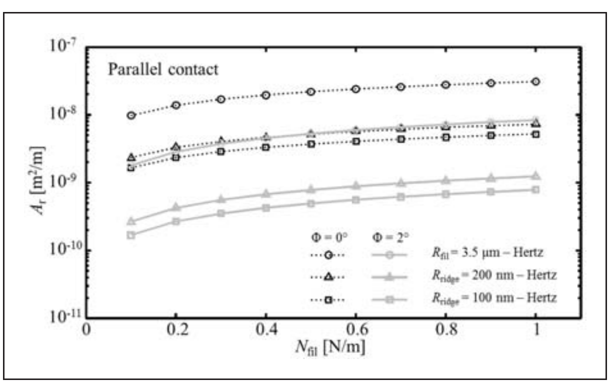

Figure 9. Contact area A_r as a function of the distributed filament load for perfectly parallel ($\Phi = 0^\circ$) and nearly parallel ($\Phi = 2^\circ$) contact of two filaments. The contact areas are shown for three different geometries: $R_{fil} = 3.5\,\mu m$ represents the smooth filament assumption, the contact of 1×1 small ridges is represented by $R_{ridge} = 100$ nm, the contact of 1×1 large ridges by $R_{ridge} = 200$ nm. The areas are shown for Hertzian contact, i.e. without adhesion contribution.

The smooth filament assumption leads to a contact area of about a factor ten higher than the predictions for ridge-to-ridge contact. Furthermore, Figure 9 shows that the real area of contact per unit filament length for the perfectly parallel contact ($\Phi = 0^\circ$) is about an order of magnitude higher than the predicted contact for a small angle $\Phi = 2^\circ$ between the stationary and moving filaments. The model results for both the perpendicular and parallel tow orientations are discussed in more detail in the discussion section.

Discussion

The expected frictional force between the contacting filaments can be predicted from equation (2). The obtained frictional force is compared with the experimental results to assess the model performance. Furthermore, several aspects of the model are discussed.

Comparison with experimental results

The model predictions are related to the experimental observations by comparing the measured frictional force $F_f = T_2 - T_1$ with a frictional force prediction based on equation (2).

The normal loads on the filaments were used to predict the frictional force for a small arc length segment $\Delta s = \Delta\theta\, R_{drum}$ of the contacting filaments:

$$\Delta F_f = \Delta A_r \tau, \tag{24}$$

where ΔA_r is the real contact area of a filament segment with length Δs. The total frictional force along the wrapped length of the filament was obtained by summation of the segment frictional forces from equation (24). The small arc length segments were $\Delta s = 2R_{fil}$ for the perpendicular contact and $\Delta s = \pi\, R_{drum}/n_{oblique}$ for the nearly parallel contact situation. The frictional force for the tow is then obtained by multiplying the number of filaments in direct contact n_{fil} with the summed frictional force $F_f = \Sigma\Delta F_f$ per filament. Figure 10 shows the results of this comparison for perpendicular contact, with (MD) and without (Hertz) the contribution of adhesion between the contacting tows. The calculations are shown for an estimated interfacial shear strength $\tau = 100$ MPa. Note that, to the authors' best knowledge, this value has not been determined with accuracy. This research does not aim to provide an accurate measure of τ, it should be considered as a ball-park figure. The particular value was based on literature citing values between 20 MPa and 100 MPa for carbon filaments sliding against different counterfaces,[16,28] with a theoretical maximum of 600 MPa being the basal plane shear strength of graphite crystals.

The frictional force prediction for the smooth filament assumption overestimates the measured friction by more than an order of magnitude and was therefore not included in the graph. The predicted frictional forces are in the same range as the experimental observations for perpendicular contact between the ridges on the carbon filaments. The contribution of adhesion to the friction is limited, due to the small radius of curvature of the contacting ridges. As indicated in the legend of the graph in Figure 10, the solid grey F_f -curve representing the Hertzian 1×1 ridge contact with $R_{ridge} = 200\,\text{nm}$ coincides with that of the 2×2 small ridge contact with $R_{ridge} = 100\,\text{nm}$.

However, for the MD-curve, i.e. taking the contribution of adhesion into account, the friction is slightly higher for the 2×2 small ridge contact than for the 1×1 large ridge contact. Thus, the effect of adhesion for one large contact is smaller than the effect for several small contacts, which have the same total Hertzian contact area. It is very likely that a mixture of 1×1, 2×2, and 1×2 contacts occurs in an actual contact situation. Although the distribution of each of the three combinations is not known, the frictional force as a result of the mixture of the aforementioned contact situations can be expected to lie close to the experimentally observed value indicated by the star symbol in Figure 10.

Figure 11 shows the results for the parallel tow contact, i.e. under a small angle $\Phi = 2°$. The Hertzian contact is shown for the same interfacial shear strength as for perpendicular contact, i.e. $\tau = 100\,\text{MPa}$. The predicted frictional force appears to be in qualitative as well as quantitative agreement with the experimentally observed value indicated by the star symbol. Thus, the modeled oblique contact at a relative angle $\Phi = 2°$ of ridges on the filaments appears to provide a good representation of the actual experiment.

The contact area ellipticity, which is the ratio of the major and the minor semi-axis of the contact ellipse, is rather high with values up to 135 for a distributed load of 1 N/m. It is likely that a deviation occurs between the shape of the modeled Hertzian and the actual filament–filament contact. Additionally, one should note that the major semi-axis dimension $b_{ell} = 8.8\,\mu\text{m}$ of the contact ellipse is of the same order of magnitude as the filament diameter for normal distributed loads around 1 N/m (for smooth filament contact; the corresponding minor semi-axis dimension $a_{ell} = 67\,\text{nm}$). For the 1×1 ridge contact, these values are $a_{ell} = 20\,\text{nm}$ and $b_{ell} = 2.7\,\mu\text{m}$. This implies that the small deformation assumption of the Hertzian contact model does not apply. A maximum contact pressure of 1.9 GPa (178 MPa) occurs for the 1×1 small ridge (smooth filament) contact with a distributed normal load of 1 N/m. In the case of the capstan experiment a maximum contact pressure of 1.5 GPa (142 MPa) can be expected for the maximum applied distributed normal load of 0.5 N/m. This seems to be a rather high pressure to still fall within the assumed elastic material deformation regime, although the exact compressive strength of carbon filaments is not known

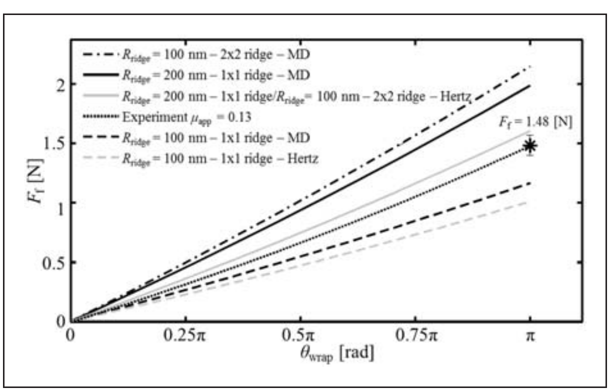

Figure 10. Predicted frictional force F_f as a function of the wrapping angle θ_{wrap} on the capstan setup for various ridge-to-ridge contact situations in a perpendicular orientation. The star symbol indicates the measured force in the experiment; the dotted line shows the frictional force based on equation (5) with $\mu_{app} = 0.13$. The Hertz curves represent the friction without adhesion contribution, whereas the MD curves account for the effect of adhesion. The frictional force curve for 2×2 ridge contact of $R_{ridge} = 100\,\text{nm}$ coincides with that of 1×1 ridge contact with $R_{ridge} = 200\,\text{nm}$ for Hertzian contact.

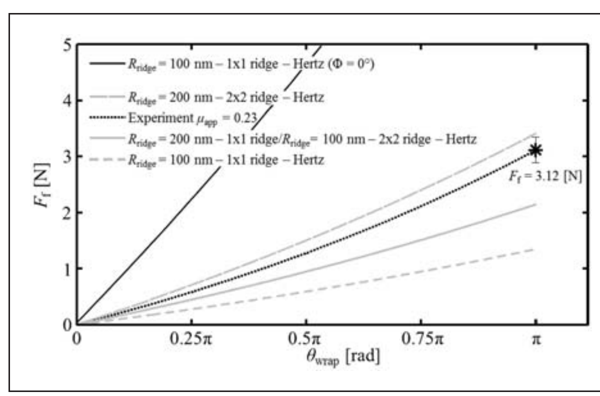

Figure 11. Predicted frictional force F_f as a function of the wrapping angle θ_{wrap} on the capstan setup for various ridge-to-ridge contact situations in nearly parallel contact, i.e. $\Phi = 2°$. The star symbol indicates the measured force in the experiment; the dotted line shows the calculated frictional force based on equation (5) with $\mu_{app} = 0.23$. The frictional force curve for 2×2 ridge contact of $R_{ridge} = 100\,\text{nm}$ coincides with that of 1×1 ridge contact with $R_{ridge} = 200\,\text{nm}$. The solid black line represents the contact for a perfectly parallel orientation of filaments, i.e. $\Phi = 0°$.

accurately to date. Altogether, it seems plausible that contact between multiple ridges occurs in the actual filament-filament contact.

The thin solid black curve in Figure 11 depicts the frictional force prediction for 1×1 ridge-to-ridge ($R_{\mathrm{ridge}} = 100\,\mathrm{nm}$) contact in perfectly parallel orientation, i.e. $\Phi = 0^{\circ}$. This clearly illustrates the overestimation of the frictional force F_{f} when a perfectly parallel orientation of the filaments is assumed. A mixture of ridge-to-ridge contact situations is expected to apply in reality, similar to the case of perpendicular contact.

Model assumptions

Several simplifying assumptions were made in the contact modeling procedure. First, a uniform distribution of the normal loads N_{fil} on each filament in the bottom layer of the stationary tow was assumed, as illustrated in Figure 3. This approximation neglects load variations at, for example, the edges of the tow, where fewer filaments are present to transmit the normal load to the bottom layer. The true value of N_{fil} is expected to vary slightly along the width of the tow. However, the current approach appears to give an adequate representation.

Second, an ideal packing of filaments in the tow was assumed, which is not the case in reality. A small amount of entangled or misaligned filaments was present in the tow material, disturbing the parallel arrangement of filaments within a tow, although the supplied tow material had no intentionally applied twist. However, these effects are very likely averaged out in the capstan experiment. Furthermore, the close packing assumption implies that there is no spacing between the filaments in the tow, thus the amount of contacting filaments in the bottom layer of the stationary tow n_{fil} is an upper bound estimate of the actual situation. Variations of n_{fil} along the wrapped length l_{wrap} of the tow are expected to occur as well, due to a varying width of the tow on the capstan drum. The effect of the tow width variation was not taken into account in the current work. Another effect that was not taken into account is the contribution of digging in of filaments of the contacting tows. This effect, where a filament is in contact with two other filaments under a wedge- like angle, is described in detail in previous work.[10] It leads to an observed apparent coefficient of friction μ_{app} of the tow on a capstan setup that is about 15% higher than the actual coefficient of friction at the filament level. However, due to the observed relative orientation of the tows, digging in is only expected to occur locally during friction experiments, i.e. at contact lengths smaller than the filament contact length on the capstan l_{wrap}. The values of μ_{app} on the tow and filament level were therefore assumed equal in this study. However, additional experimental work should be performed to rule out or confirm the presence of significant digging in of filaments.

Third, the large contact lengths between ridges on the filaments for the parallel and oblique contact cases might suggest that the surface roughness varies significantly within the contact length. In fact, mainly the large wavelengths of the surface roughness would influence the roughness significantly. However, the relatively low bending rigidity of the filaments will compensate for this wavelength, leaving the measured roughness and thus the ridged structure dominant in the analysis. The discontinuous nature of the ridges is most likely averaged out due to the large number of contacts.

Future work should focus on the assumptions regarding the amount of filaments in oblique contact n_{oblique} and the corresponding contact load P_{par}. Furthermore, the effects of small amounts of twist in the tow were not taken into account. The filaments of twisted tows in contact have a different relative contact angle Φ than those in the currently assumed parallel arrangement of filaments within the tows. The modeling approach in this work was presented for carbon tow material; however, the frictional behavior of any fibrous material can be modeled using this approach as long as the surface characteristics of the filaments are taken into account in the modeling approach.

Conclusions

A contact mechanics model for the prediction of the friction between sliding tows has been developed. The model accounts for the difference in frictional behavior between perpendicular and nearly parallel relative tow orientations. An agreement on the order of magnitude level was found between the contact model and observations from capstan experiments. The results of this research are limited to this order of magnitude level due to the uncertain value of the interfacial shear strength τ and the simplifications in the assumptions behind the proposed modeling approach.

Because the approximation of a smooth filament surface led to an overestimation of the frictional force between sliding tows, the surface characteristics of carbon filaments were taken into account. This resulted in a good agreement between the contact model and the experimental results in the case of perpendicular and nearly parallel contact between tows. The contact area and hence the frictional force in the tow were overestimated for perfectly parallel contact of the filaments in the tow. Further investigation of the contact and load assumptions are required for an improved prediction of the frictional behavior of sliding fibrous tows with, for example, intentionally applied twist. The current modeling approach should support the prediction of all relative tow orientations. Additional experiments at intermediate relative tow orientations can further improve the physical understanding of tow-tow friction and confirm the validity of the proposed modeling approach.

The contact model in this work provides an approximate (order of magnitude) physical explanation for the experimentally observed orientation dependence of tow friction. The mesoscopic frictional behavior of fibrous tows was explained by taking microscopic characteristics of the constituents into account.

The orientation-dependent frictional behavior of fibrous tows was assessed on a mesoscopic level. The frictional behavior of textile reinforcements like woven fabrics is typically assessed on the macroscopic ply level. The insights on the level of fibrous tows can thus provide a coupling between the macroscopic deformation of a textile reinforcement and the resulting deformations on the microscopic filament level.

Funding

This study was supported by the Stichting Technologie en Wetenschap (STW) van der Leeuw (grant number STW-06182).

Acknowledgments

The authors wish to thank Ten Cate Advanced Composites and vom Baur for their support and supply of testing materials.

References

1. Cornelissen B, de Rooij MB, Rietman B, et al. Frictional behaviour of high performance fibrous tows: a contact mechanics model of tow–metal friction. *Wear* 2013; 305: 78–88.
2. Huffington JD and Stout HP. The friction of fibre assemblies. *Wear* 1960; 3: 26–42.
3. Nikonova EA and Pakshver AB. The friction properties of textile yarns. *Fibre Chem* 1973; 4: 657–660.
4. Robins MM, Rennell RW and Arnell RD. The friction of polyester textile fibres. *J Phys D Appl Phys* 1984; 17: 1349–1360.
5. Briscoe BJ and Motamedi F. Role of interfacial friction and lubrication in yarn and fabric mechanics. *Text Res J* 1990; 60: 697–708.
6. Leech CM. The modelling of friction in polymer fibre ropes. *Int J Mech Sci* 2002; 44: 621–643.
7. Rubenstein C. Review on the factors influencing the friction of fibres, yarns and fabrics. *Wear* 1959; 2: 296–310.
8. Potluri P and Atkinson J. Automated manufacture of composites: handling, measurement of properties and lay-up simulations. *Composites Part A* 2003; 34: 493–501.
9. Yuksekkaya ME. More about fibre friction and its measurements. *Text Prog* 2009; 41: 141–193.
10. Cornelissen B, Rietman B and Akkerman R. Frictional behaviour of high performance fibrous tows: Friction experiments. *Composites Part A* 2013; 44: 95–104.
11. Howell HG and Mazur J. Amontons' law and fibre friction. *J Text Inst Trans* 1953; 44: T59–T69.
12. Gupta BS and El Mogahzy YE. Friction in fibrous materials. Part I: Structural model. *Text Res J* 1991; 61: 547–555.
13. Grishanov SA. Fundamental modelling of textile fibrous structures. In: Chen X (ed.) *Modelling and predicting textile behaviour*. Woodhead Publishing, 2010, pp.41–111.
14. El Mogahzy YE and Gupta BS. Friction in fibrous materials. Part II: Experimental study of the effects of structural and morphological factors. *Text Res J* 1993; 63: 219–230.
15. Roselman IC and Tabor D. The friction of carbon fibres. *J Phys D Appl Phys* 1976; 9: 2517–2532.
16. Roselman IC and Tabor D. The friction and wear of individual carbon fibres. *J Phys D Appl Phys* 1977; 10: 1181–1194.
17. Ueda M and Takiguchi T. Measurement of transverse Young's modulus of carbon fibres by angular characteristics of ultrasonic scattering. In: *Proceedings of the IEEE 1990 Ultrasonics Symposium, Vol. 2*, Honolulu, HI. IEEE, 1990, pp.1081–1085.
18. Maurin R, Davies P, Baral N, et al. Transverse properties of carbon fibres by nano-indentation and micromechanics. *Appl Compos Mater* 2008; 15(2): 61–73.
19. Luo Y, Zhao Y, Duan Y, et al. Surface and wettability property analysis of CCF300 carbon fibers with different sizing or without sizing. *Mater Des* 2011; 32: 941–946.
20. Shackelford JF. *Introduction to materials science for engineers*, 4th ed. Prentice-Hall, 1996.
21. Johnson KL. Contact mechanics. 9th ed. Cambridge University Press, Cambridge, UK, 1985.
22. Maugis D. Adhesion of spheres: the JKR–DMT transition using a Dugdale model. *J Colloid Interface Sci* 1992; 150: 243–269.
23. Johnson KL and Greenwood JA. An adhesion map for the contact of elastic spheres. *J Colloid Interface Sci* 1997; 192: 326–333.
24. Barthel E. Adhesive elastic contacts: JKR and more. *J Phys D Appl Phys* 2008; 41(16): 1–20.
25. Hertz H. Ueber die Berührung fester elastischer Körper. *J Reine Angew Math* 1881; 92: 156–171.
26. Moes H. *Lubrication and beyond*, University of Twente. www.utwente.nl/ctw/tr/Research/Publications/Books (2000, accessed 11 September 2012).
27. Sümer B, Onal CD, Aksak B, et al. An experimental analysis of elliptical adhesive contact. *J Appl Phys* 2010; 107(11): 1–7.
28. Adams MJ, Briscoe BJ, Law JYC, et al. Influence of vapor condensation on the adhesion and friction of carbon-carbon nanocontacts. *Langmuir* 2001; 17: 6953–6960.

Appendix 1.Derivation of the normal tow load

Figure 12 depicts the loads on a small part of the tensioned wrapped tow on the counterface. The normal load in unit Newton is expressed as the product of the normal stress component σ with the projected area formed by $tR_{\mathrm{drum}}d\theta$, where t is the local tow width and $R_{\mathrm{drum}}d\theta$ is the arc length of the tow section. The vertical force equilibrium $\Sigma F_{\mathrm{y}} = 0$ in the tow section then yields:

$$\sigma t R_{\mathrm{drum}} d\theta - T(\theta + d\theta)\sin\left(\frac{d\theta}{2}\right) - T(\theta)\sin\left(\frac{d\theta}{2}\right) = 0. \tag{25}$$

The term $\sin(d\theta/2) \approx d\theta/2$ for infinitesimally small $d\theta$. Likewise, dT is small, so $T(\theta + d\theta) \approx T(\theta)$. Then, the following equilibrium exists:

$$\sigma t R_{\mathrm{drum}} d\theta = 2T(\theta)\frac{d\theta}{2}. \tag{26}$$

Bringing the arc length $R_{\mathrm{drum}}d\theta$ to the right-hand side of equation (26) gives the distributed normal load $N_{\mathrm{tow}}(\theta) = \sigma t$ in unit N/m arc length:

$$N_{\mathrm{tow}}(\theta) = \frac{T(\theta)}{R_{\mathrm{drum}}}. \tag{27}$$

Thus, the local distributed normal load on the wrapped tow was derived using the tensile load in the tow and the capstan drum geometry.

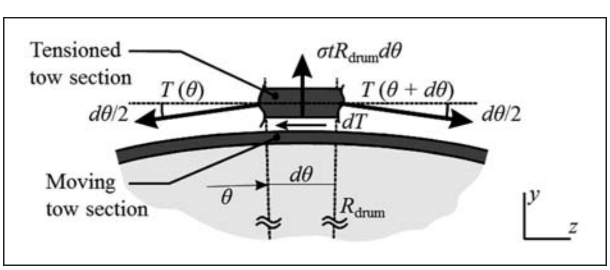

Figure 12. Schematic illustration of the tow–tow contact on the capstan friction drum. The bottom or moving tow is attached to the rotating drum, the tensioned, stationary tow is wrapped around the drum; a sliding contact is formed.

Appendix 2. Maugis–Dugdale adhesive contact calculations

This appendix presents the approach to obtain the contact area between filaments in a perpendicular orientation, accounting for adhesion effects. The equivalent radius of curvature R_{m} is determined from the cylindrical bodies with $R_{\mathrm{y1}} = R_{\mathrm{y2}} = \infty$ and $R_{\mathrm{x1}} = R_{\mathrm{x2}}$ is determined by R_{fil} or R_{ridge}, depending on the smooth or ridge- containing filament surface description, respectively. The equivalent radius of curvature R_{m} and the reduced elasticity modulus E^* are defined as:

$$\begin{aligned} R_{\mathrm{m}} &= \left(\frac{1}{R_{\mathrm{x1}}} + \frac{1}{R_{\mathrm{y1}}} + \frac{1}{R_{\mathrm{x2}}} + \frac{1}{R_{\mathrm{y2}}}\right)^{-1}, \\ E^* &= \left(\frac{1-\nu_1^2}{E_1} + \frac{1-\nu_2^2}{E_2}\right)^{-1}. \end{aligned} \tag{28}$$

The following non-dimensional parameters are introduced to facilitate the contact calculations:[23]

$$\begin{aligned} \bar{a} &\equiv a_{\mathrm{MD}}\left(\frac{E^*}{3\pi w R_{\mathrm{m}}^2}\right)^{1/3}, \\ \bar{c} &\equiv c_{\mathrm{MD}}\left(\frac{E^*}{3\pi w R_{\mathrm{m}}^2}\right)^{1/3}, \\ \bar{\delta} &\equiv \delta_{\mathrm{MD}}\left(\frac{8E^{*2}}{9\pi^2 w^2 R_{\mathrm{m}}}\right)^{1/3}, \\ \bar{P} &\equiv \frac{P_{\mathrm{perp}}}{2\pi w R_{\mathrm{m}}}, \end{aligned} \tag{29}$$

where w is the work of adhesion listed in Table 1 and P_{perp} represents the contact load in newtons. The dimensionless parameter $\overline{P}$ is the ratio between P_{perp} and the adhesive pull-off force $2\pi w R_{\mathrm{m}}$ required to separate the contacting bodies. The intimate contact radius is represented by a_{MD}, the radius c_{MD} represents the extent to which the maximum attractive force due to surface interactions $\sigma_0 = w/(0.97z_0)$ acts. Here, z_0 is the interatomic or intermolecular equilibrium spacing.[23] The transition parameter λ is a measure of the ratio of elastic deformation to the range of surface forces and is defined as:[23]

$$\lambda \equiv \left(\frac{w}{0.97z_0}\right)\left(\frac{9R_{\mathrm{m}}}{\pi w E^{*2}}\right)^{1/3}. \tag{30}$$

The following nonlinear system of equations is solved numerically to obtain the contact parameters being the dimensionless intimate contact radius $\overline{a}$ and the dimensionless radius of adhesion $\bar{c}$, respectively, with $m = c_{MD}/a_{MD}$:[22,23]

$$\begin{aligned}
&\frac{\lambda\bar{a}^2}{2}\left[\left(m^2-2\right)\arccos\left(\frac{1}{m}\right)+\sqrt{m^2-1}\right] \\
&\quad+\frac{4\lambda^2\bar{a}}{3}\left[\sqrt{m^2-1}\ \arccos\left(\frac{1}{m}\right)-m+1\right]=1, \\
&\bar{\delta}=\bar{a}^2-\frac{4\lambda\bar{a}}{3}\sqrt{m^2-1}, \\
&\bar{P}=\bar{a}^3-\lambda\bar{a}^2\left[\sqrt{m^2-1}+m^2\ \arccos\left(\frac{1}{m}\right)\right].
\end{aligned} \tag{31}$$

The absolute dimension of the circular contact area A_{MD} is then obtained from the radius of the contact area a_{MD} in equation (29):

$$A_{MD} = \pi\, a_{MD}^2. \tag{32}$$

Appendix 3.General Hertzian elliptic contact

The dimensionless parameters α, β, and γ account for the ellipticity of the contact between bodies in an oblique orientation ($\Phi \neq 0$):

$$\begin{aligned}
\alpha &= \kappa^{1/3}\left[\frac{2}{\pi}\mathbf{E}(m)\right]^{1/3}, \\
\beta &= \kappa^{-2/3}\left[\frac{2}{\pi}\mathbf{E}(m)\right]^{1/3}, \\
\gamma &= \kappa^{2/3}\left[\frac{2}{\pi}\mathbf{E}(m)\right]^{-1/3}\frac{2}{\pi}\mathbf{K}(m).
\end{aligned} \tag{33}$$

The ellipticity ratio $\kappa = a_{ell}/b_{ell}$ for $a_{ell} < b_{ell}$ is approximated by:

$$\kappa \approx \left[1+\sqrt{\frac{\ln 16/\zeta}{2\zeta}-\sqrt{\ln 4}+0.16\ln\zeta}\right]^{-1}, \tag{34}$$

$$\zeta = \frac{R_Y}{R_X} \quad \text{with } 0 < \zeta \leq 1. \tag{35}$$

The complete elliptic integrals of the first and second kind $\mathbf{K}(m)$ and $\mathbf{E}(m)$, respectively are approximated by:[26]

$$\mathbf{K}(m) \approx \frac{\pi}{2}(m-1)\left[1+\frac{2m}{\pi(1-m)}\ln\left(\frac{4}{\sqrt{1-m}}\right)-\frac{3}{8}\ln(1-m)\right], \tag{36}$$

$$\mathbf{E}(m) \approx \frac{\pi}{2}(m-1)\left[1+\frac{2m}{\pi(1-m)}-\frac{1}{8}\ln(1-m)\right], \tag{37}$$

with $m = 1-\kappa^2$. $\mathbf{K}(m)$ and $\mathbf{E}(m)$ were solved numerically using Matlab, the variations with respect to the approximations in equations (36) and (37) were within 0.25%.